RESEARCH ARTICLE | OCTOBER 24 2007

Two-dimensional inviscid pinch-off: An example of self-similarity of the second kind

J. C. Burton; P. Taborek

Physics of Fluids 19, 102109 (2007)
https://doi.org/10.1063/1.2800387

Two-dimensional inviscid pinch-off: An example of self-similarity of the second kind

J. C. Burton and P. Taborek
Department of Physics and Astronomy, University of California, Irvine, California 92697, USA

(Received 27 June 2007; accepted 28 September 2007; published online 24 October 2007)

The pinch-off of a two-dimensional region of inviscid fluid is investigated using numerical and analytical techniques. We find that pinch-off occurs when a sufficiently deformed 2D drop is released from rest. The asymptotic collapse of the pinching region is characterized by an anomalous, nonrational similarity exponent α, indicating the existence of self-similarity of the second kind. Numerical solutions of the boundary integral equations show that the height of the pinch region shrinks faster than the width, so that the singularity can be described by a slender approximation. The partial differential equations obtained from this approximation are solved and are consistent with the full boundary integral methods. Furthermore, by casting the partial differential equations into similarity form, we solve a nonlinear eigenvalue problem to obtain the value of the similarity exponent, $\alpha=0.6869\pm0.0003$. © *2007 American Institute of Physics*. [DOI: 10.1063/1.2800387]

I. INTRODUCTION

Singularity formation and topology changes in free surface flows and fluid sheets have been the subject of extensive research in the fluid dynamics field for the last two decades. One of the motivations for this work is the particularly close connection to some of the simplest and most commonly observed fluid phenomena, such as water dripping from a faucet. The ease of experimental access to these simple physical systems with a finite time singularity has facilitated careful comparison between theory and experiment. Another important driving factor for research in this field has been the challenge of mathematically describing and classifying the possible types of "pinch-off" singularities.[1] The solutions of the equations describing pinch-off often have a self-similar form with unique power law exponents describing the collapse or divergence of quantities such as neck thickness, velocity, and pressure. The large majority of research has focused on pinch-off in 3D axisymmetric droplets in different flow regimes (inviscid flow, Stokes' flow). A notable example is the solution found by Eggers[2] for the pinch-off of an axisymmetric fluid thread where surface tension, viscosity, and inertia are all of comparable importance. Eggers showed that the asymptotic power law exponents are rational numbers which can be predicted by a dimensional analysis of the fluid parameters and geometry of the problem. Rational exponents derivable from dimensional considerations are a hallmark of self-similarity of the first kind. In many cases, however, the asymptotic behavior is more complicated. When the similarity exponent cannot be predicted from dimensional analysis alone, the solution is then described as "self-similarity of the second kind," a term first used by Barenblatt.[3] One example of this type of self-similarity is discussed in Ref. 4 and then in Ref. 5 for the Stokes' flow pinch-off of an axisymmetric fluid thread.

For the case of inviscid pinch-off of a 3D axisymmetric droplet, experiments and simulations[6–12] yield a similarity exponent of exactly 2/3. This is the result expected from simple dimensional analysis using the surface tension σ and the fluid density ρ as the relevant parameters, $L\sim(\sigma/\rho)^{1/3}T^{2/3}$, where L and T are the characteristic length and time associated with the singularity. If we apply the same reasoning to the problem of 2D inviscid pinch-off with line tension λ and 2D density ξ, then the exponent which describes the time dependence of the characteristic length is again 2/3, with $L\sim(\lambda/\xi)^{1/3}T^{2/3}$. Our recent experiments with pinch-off in low-viscosity, quasi-2D liquid lens systems[13] show that simple changes in the geometry of the fluid (thin liquid lens versus axisymmetric drop) result in drastic changes to the structure and nature of the singularities. The results reported in this article were motivated by an attempt to understand how inviscid pinch-off differs in 2D and 3D.

Although simple dimensional arguments suggests that the characteristic exponents do not depend on the spatial dimension of the fluid, the capillary stability of a fluid region to small perturbations is quite different in 2D and 3D. The early stage of pinch-off in 3D is typically driven by surface tension. A sufficiently deformed axisymmetric droplet begins to break apart due to the positive radial curvature κ_r near $z=0$ in the (r,θ) plane (Fig. 1). The axial curvature κ_z in the (r,z) plane is negative, and tends to pull the drop back into a spherical shape. When the mean curvature $\kappa_m=1/2(\kappa_r+\kappa_z)$ near a thin neck is positive, the drop is unstable and begins to break into two pieces. In 2D, there is no analog of "radial curvature." There is only one curvature κ_x (analog of κ_z), which must be negative near a minimum neck thickness, so curvature induced Laplace pressure cannot be the driving force for pinch-off in 2D. This suggests that pinch-off may not be possible in 2D. We have found, however, that sufficiently deformed 2D droplets released from rest do indeed undergo pinch-off. Qualitatively, this is due to the Bernoulli pressure caused by the large fluid velocities which arise as the line tension potential energy is converted into kinetic energy of flow. This effect apparently overwhelms the

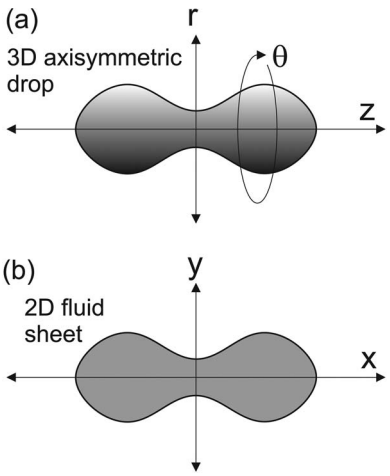

FIG. 1. (a) Cartoon of a deformed 3D axisymmetric droplet. The surface of the 3D drop is obtained by rotating the boundary around the z-axis; it is characterized by two curvatures, κ_r and κ_z. (b) Cartoon of a 2D fluid drop. In 2D, the fluid sheet lies entirely in the (y,x) plane, and is characterized by a single curvature κ_x.

Laplace curvature term and the sheet begins to pinch and eventually follows a self-similar solution. We have studied the pinching flows using three different techniques. In Sec. II, we describe numerical solutions of the boundary-integral equations for potential flow of deformed drops in both 2D and 3D. In 3D, our code reproduces the well known solutions obtained previously by others.[7–9] The 2D and 3D calculations differ primarily in the form of the Green's function used, but the 2D case produces a qualitatively different shape of the pinch region and different (irrational) power laws which describe the rate of collapse of the neck. Another important difference between the solutions in the 2D and 3D cases is the way in which the characteristic axial and radial length scales vary with time. In 3D, axial and radial lengths have the same time dependence, so the shape of the neck is self-similar. In 2D, however, the characteristic radial length shrinks faster than the axial length, so the profile is not self-similar, and variations of the flow properties in the radial direction become asymptotically negligible compared to variations in the axial direction. This allows a simplification of the equations of motion known as the slender approximation. In Sec. III, the partial differential equations for the neck profile in the slender approximation are solved numerically. These equations are simpler and computationally much more efficient than the boundary integral solutions, but the same basic result of irrational exponents and different scaling behavior in the radial and axial directions are obtained. In Sec. IV, the slender approximation equations are converted to a system of ordinary differential equations by assuming a scaling form of solution involving an exponent α. The boundary conditions on the ODEs yield a nonlinear eigenvalue problem which determines a unique value for α. The scaling form of the solutions leads to power laws for the neck profile which are in excellent agreement with the other two methods of solution.

II. BOUNDARY-INTEGRAL SIMULATIONS

We begin with an initial boundary of a 3D axisymmetric drop in the (r,z) plane or the boundary of a 2D sheet in the (y,z) plane (Fig. 1). A typical simulation starts with a dumbbell shaped domain at rest ($\vec{\mathbf{v}}=0$ everywhere). The shape is then acted upon by surface tension (3D) or line tension (2D) forces occurring at the boundary. Our simulations are restricted to perfectly inviscid, incompressible fluids with smooth, nonturbulent flows. In this regime, standard potential flow theory can be applied where a potential $\phi(\vec{\mathbf{x}}_o)$ is specified along the boundary, and $\nabla^2\phi(\vec{\mathbf{x}})=0$ everywhere. The normal component of the velocity along the boundary can then be calculated through boundary integral equations. However, the resulting integral equations are weakly singular, which can pose a computational difficulty.[14] A method for singularity reduction in the integrals is given by Nie and Baker,[15] which involves describing the flow by a dipole distribution $q(\vec{\mathbf{x}}_o)$ along the surface, and along with $\phi(\vec{\mathbf{x}}_o)$, introducing the vector potential $\vec{\mathbf{A}}(\vec{\mathbf{x}}_o)$. The resulting integral equations are

$$q(\vec{\mathbf{x}}_o) = \int_B [q(\vec{\mathbf{x}}) - q(\vec{\mathbf{x}}_o)]\vec{\nabla}G(\vec{\mathbf{x}}_o,\vec{\mathbf{x}})\cdot\vec{\mathbf{n}}(\vec{\mathbf{x}})ds(\vec{\mathbf{x}}) - \phi^-(\vec{\mathbf{x}}_o), \tag{1}$$

$$\vec{\mathbf{A}}(\vec{\mathbf{x}}_o) = \int_B [q(\vec{\mathbf{x}}) - q(\vec{\mathbf{x}}_o)]\vec{\mathbf{n}}(\vec{\mathbf{x}})\times\vec{\nabla}G(\vec{\mathbf{x}}_o,\vec{\mathbf{x}})ds(\vec{\mathbf{x}}), \tag{2}$$

where $\vec{\mathbf{n}}(\vec{\mathbf{x}})$ is the normal vector pointing away from the fluid and $G(\vec{\mathbf{x}}_o,\vec{\mathbf{x}})$ is the free space Green's function in the appropriate dimension,

$$G_{2D}(\vec{\mathbf{x}}_o,\vec{\mathbf{x}}) = -\frac{1}{2\pi}\ln|\vec{\mathbf{x}}-\vec{\mathbf{x}}_o|,$$
$$G_{3D}(\vec{\mathbf{x}}_o,\vec{\mathbf{x}}) = \frac{1}{4\pi}|\vec{\mathbf{x}}-\vec{\mathbf{x}}_o|^{-1}. \tag{3}$$

In this formulation, the potential has a discontinuous jump across the boundary,

$$\phi^+ - \phi^- = q, \tag{4}$$

where the superscript denotes the exterior $(+)$ and interior $(-)$ side of B. The value of the potential exactly on the boundary is taken as the principal value of ϕ,

$$\phi^{PV} = \tfrac{1}{2}(\phi^+ + \phi^-). \tag{5}$$

In 2D, Eqs. (1) and (2) are line integrals over the boundary of the sheet, and in 3D, the integral is taken over the surface of the axisymmetric drop. However, the axisymmetry in 3D can be exploited by performing the azimuthal (θ) integration analytically,[15] which reduces 1 and 2 to line integrals in the (r,z) plane (Fig. 1). The boundary was discretized by a collection of marker points, and quintic splines were used calculate derivatives and to interpolate between points. We have restricted ourselves to boundaries that are symmetric about the r-axis (y-axis) and the z-axis (x-axis) in 3D (2D). Because of this, we only need marker points in one quadrant,

which speeds up the calculations. The boundary integrals were calculated using an 8-point Gaussian quadrature. Once $\phi^-(\vec{\mathbf{x}}_o)$ is specified at each marker point, Eq. (1) can be solved efficiently by the method of successive substitutions to obtain the values of $q(\vec{\mathbf{x}}_o)$ along the boundary. $\vec{\mathbf{A}}(\vec{\mathbf{x}}_o)$ can then be obtained by a direct integration of $q(\vec{\mathbf{x}}_o)$. To obtain the normal component of the velocity along the boundary, we make use of the fact that $\vec{\mathbf{n}}\cdot\vec{\mathbf{v}}=\vec{\mathbf{n}}\cdot\vec{\nabla}\phi^-=\vec{\mathbf{n}}\cdot(\vec{\nabla}\times\vec{\mathbf{A}})$. It turns out that $\vec{\mathbf{n}}\cdot(\vec{\nabla}\times\vec{\mathbf{A}})$ can be calculated using only derivatives along the boundary, which are easily obtained by direct differentiation of $\vec{\mathbf{A}}$. Although the normal component of the velocity must be continuous across B, the tangential component of the velocity undergoes a discontinuous jump across B. We chose to advect the marker points on the boundary using the velocity obtained from the principal value of the potential [Eq. (5)],

$$\frac{D\vec{\mathbf{x}}}{Dt}=\vec{\mathbf{v}}, \tag{6}$$

where $D/Dt=\partial/\partial t+(\vec{\nabla}\phi^{\mathrm{PV}}\cdot\vec{\nabla})$ is the convective derivative. Since there is no external fluid in our problem, we only need the time evolution of the internal potential ϕ^-, which is governed by the kinematic boundary condition

$$\frac{D\phi^-}{Dt}=\frac{1}{2}|\vec{\nabla}\phi^-|^2+\frac{1}{2}(\vec{\nabla}\phi^-\cdot\vec{\mathbf{s}})(\vec{\nabla}q\cdot\vec{\mathbf{s}})+(P^+-P^-), \tag{7}$$

where $\vec{\mathbf{s}}$ is the unit vector tangent to the boundary and (P^+-P^-) is the pressure difference across the boundary. In 2D, this pressure difference is given by $(P^+-P^-)=\lambda\kappa_x/\xi$, where λ is the line tension, ξ is the 2D density of the fluid, and κ_x is the curvature of the boundary in the (x,y) plane. In 3D, the pressure difference depends on the two principal radii of curvature for the surface, $(P^+-P^-)=\sigma(\kappa_r+\kappa_z)/\rho$, where σ is the surface tension, ρ is the 3D fluid density, κ_z is the axial curvature in the (r,z) plane, and κ_r is the radial curvature which lies in a plane perpendicular to the (r,z) plane and contains the normal vector pointing outward from the surface.

For simplicity, all fluid parameters were set equal to unity for most simulations. Using an explicit fourth-order Runge-Kutta scheme, the x and y coordinates of each marker point and the value of ϕ^- at each point were advanced in time. As the singularity was approached, refinement of the grid of marker points and adaptive time stepping were necessary to maintain resolution at small length and time scales. In a similar fashion to the methods employed in Refs. 7 and 8 the marker points were redistributed at each time step along the boundary with the local point spacing being determined by the following formula:

$$\begin{aligned}\Delta l_{2\mathrm{D}} &\propto \arctan(\sqrt{A(x-x_{\min})^2+By^2}),\\ \Delta l_{3\mathrm{D}} &\propto \arctan(\sqrt{A(z-z_{\min})^2+Br^2}),\end{aligned} \tag{8}$$

where the subscript min denotes the position of the minimum neck thickness and A and B are numerical constants chosen according to the problem. In 3D, both horizontal and vertical lengths scale with the same exponent, so $A=B$. However, in 2D, we found that the horizontal and vertical lengths scale differently, so that A and B were adjusted as the singularity evolved. The arctan function was chosen because its value remains finite as the argument approaches infinity, so that points far away from the singularity would still retain a local spacing fine enough to accurately describe the surface. Points were added to the boundary when the local point spacing near the pinch was too large ($\delta l>0.1y_{\min}$ or $\delta l>0.1r_{\min}$). A typical number of marker points at the beginning of the simulation was ~200, whereas near the final stages of pinch-off, there were ~400 marker points. The time step δt was chosen according to the formula $\delta t=Cr_{\min}^{3/2}$ for the 3D case, and $\delta t=Cy_{\min}^{1/0.687}$ for the 2D case, where $C\sim0.1$ is a numerical constant. For 3D simulations, the value of the similarity exponent is already known to be 2/3, so that a time step proportional to $r_{\min}^{3/2}$ should scale appropriately as $\tau\to0$. Since the similarity exponent in 2D was not known *a priori*, very small time steps were taken until a good approximation of the similarity exponent was obtained so that we could make use of $\delta t=Cy_{\min}^{1/0.687}$ as the time step towards pinch-off. Typical simulations took approximately 5 days to complete on a 2 GHz desktop PC. The main results of the boundary-integral simulations for both 2D sheets and 3D droplets can be seen in Fig. 2. First, a series of boundary shapes show the approach to pinch-off for both cases. The regridding of the marker points can be seen in both the 2D and 3D cases in Fig. 2(a). In both 3D and 2D, initial conditions which are small deviations from the equilibrium shape result in oscillations (discussed in more detail in the Appendix), while sufficiently deformed initial shapes lead to pinch-off. The two cases differ in the balance of forces in the initial stages of pinch-off; in 3D, if the total curvature is positive, the Laplace pressure term tends to decrease the neck diameter, while in 2D, the Laplace pressure term always tends to increase the neck diameter. This difference in the initial stability accounts for the fact that more highly elongated initial shapes are required to induce pinch-off in 2D than in 3D. The highly elongated 2D initial shapes contained large amounts of potential line tension energy. As the drop rebounds [Fig. 2(a), right panel], the potential energy is converted into kinetic energy. The resulting large velocities create areas of low pressure, which drive a Bernoulli "suction" effect, pulling the neck of the droplet inward towards the x-axis. In 2D and 3D as the neck collapses, fluid is driven from the center mass of fluid to the large reservoirs at the ends, so the horizontal components of the velocity v_x and v_z near the singularity point away from the origin in Fig. 2(a). In 2D, the curvature is always negative near a minimum neck thickness, which means that line tension always acts to increase the neck diameter. However, in 3D, the situation is more complicated because the mean curvature $\kappa_m=1/2(\kappa_z+\kappa_r)$ changes sign near the minimum, so that different parts of the neck are being pulled in different directions by the Laplace pressure. In fact, at the minimum radius, the mean curvature is positive, meaning that the Laplace pressure helps to squeeze the neck at $r=r_{\min}$. Figures 3(a) and 3(b) show plots of the curvature near the minimum neck thickness which illustrates this point.

A zoomed-in view of the pinch region in Fig. 2(b) shows

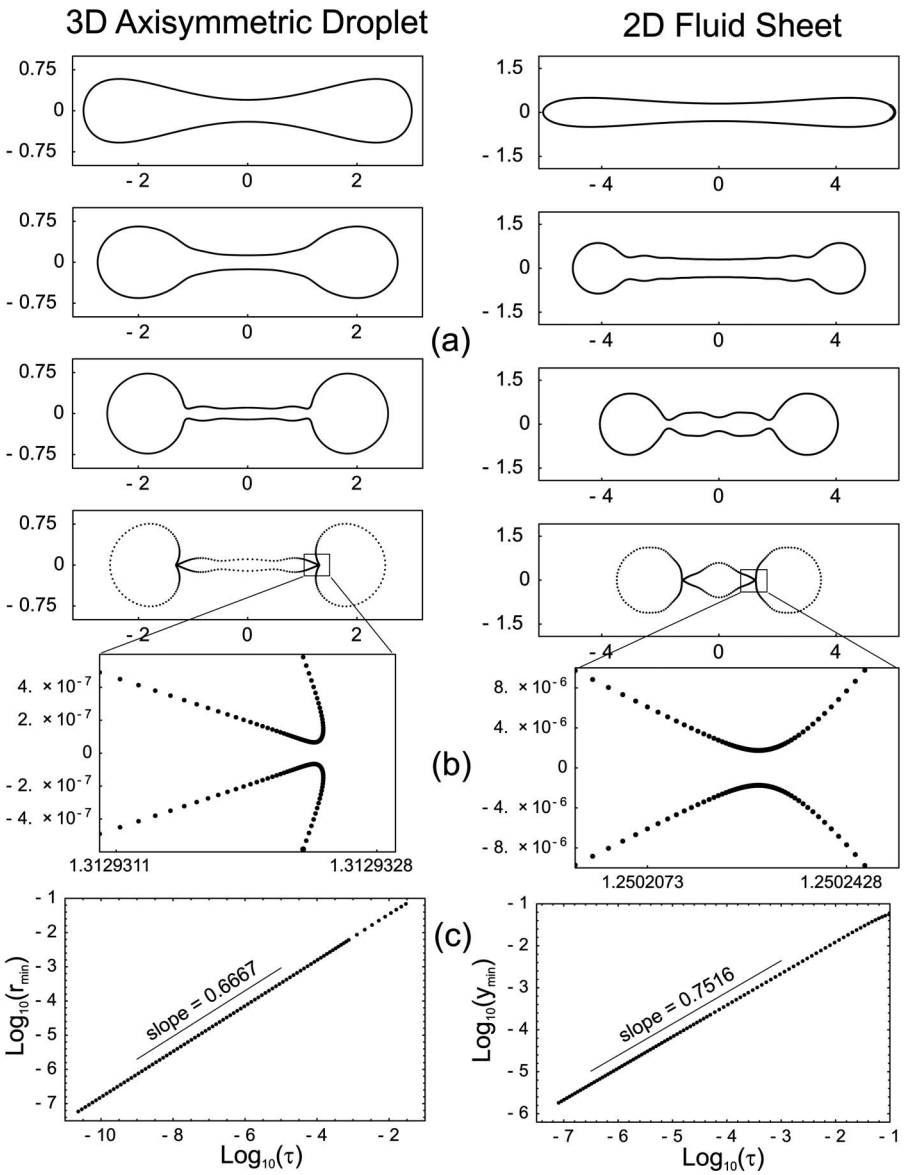

FIG. 2. (a) Sequence of boundary profiles in inviscid pinch-off for 2D (right-hand panels) and 3D (left-hand panels). The boundary initially starts at rest and is acted upon by line tension or surface tension. (b) Profile of the asymptotic pinch-off region in 2D (right) and 3D (left). The aspect ratio for the 3D plot is equal to unity, whereas the aspect ratio for the 2D plot has been enhanced to ~3.5 due to the slenderness of the pinch profile. The overturned double cone structure is realized in the 3D pinch, while in 2D, there is no overturning of the profile. (c) Log_{10}-Log_{10} plots of the minimum neck thickness ($y_{\min}$ and $r_{\min}$) as a function of the time remaining until pinch-off τ. Dimensional analysis predicts a 2/3 exponent for both 2D and 3D, but the anomalous exponent 0.7516 in 2D indicates self-similarity of the second kind.

the structure of the singularities in 2D and 3D. In 3D, an overturned, double-cone profile is always realized near pinch-off, starting from a wide array of initial conditions. The value of the cone angles are approximately 18° and 113°.[7–9] In 2D, the singular region has no overturning and looks more like an asymmetric hyperbola. The dimensional analysis of both the 3D and 2D inviscid pinch-off yields a value of 2/3 for the power law describing the time dependence of the minimum neck radius: $r_{\min} \propto (\sigma/\rho)^{1/3}\tau^{2/3}$ in 3D and $y_{\min} \propto (\lambda/\xi)^{1/3}\tau^{2/3}$ in 2D. The left panel of Fig. 2(c) shows excellent agreement with this prediction in 3D, which is essentially a verification of our numerical code since this exponent has been previously verified by simulations and experiments.[6–12,16] The first indication that 2D inviscid pinch-off does not display self-similarity of the first kind is the fact that $y_{\min}$ follows a power law in time with an anomalous exponent that is different from the predicted 2/3 obtained from dimensional analysis. The right panel in Fig. 2(c) shows the best fit exponent to the data to be 0.7516. Furthermore, in contrast to the $\tau^{2/3}$ scaling in both the horizontal and vertical lengths scales in 3D pinch-off, the height of the pinch region in 2D ($y_{\min}$) shrinks faster than the width of the pinch region (κ_x^{-1}), so that the profile becomes slender as $\tau \to 0$. This is illustrated in Fig. 3(c), which shows the ratio of the vertical to horizontal length scale Λ at the minimum neck thickness ($\Lambda = \kappa_x y|_{y=y_{\min}}$ in 2D, $\Lambda = \kappa_z r|_{r=r_{\min}}$ in 3D) as a function of τ. In 3D, this ratio approaches a constant value, which indicates that both lengths scale with the same exponent. However, this is clearly not the case for 2D pinch-off, which implies that the axial and radial scaling behavior are different. Slender approximations to many pinch-off phenomena[2,4,17–19] have been utilized to more easily study the asymptotic properties of these singularities, and an application to 2D inviscid pinch-off is the subject of the next section.

III. SLENDER APPROXIMATION

When the neck region of the pinch-off becomes slender, the equations of motion simplify considerably. Only the tangential component of the velocity $v_x(x,t)$ is retained, and the expression for the curvature is reduced to $d^2h(x,t)/dx^2$,

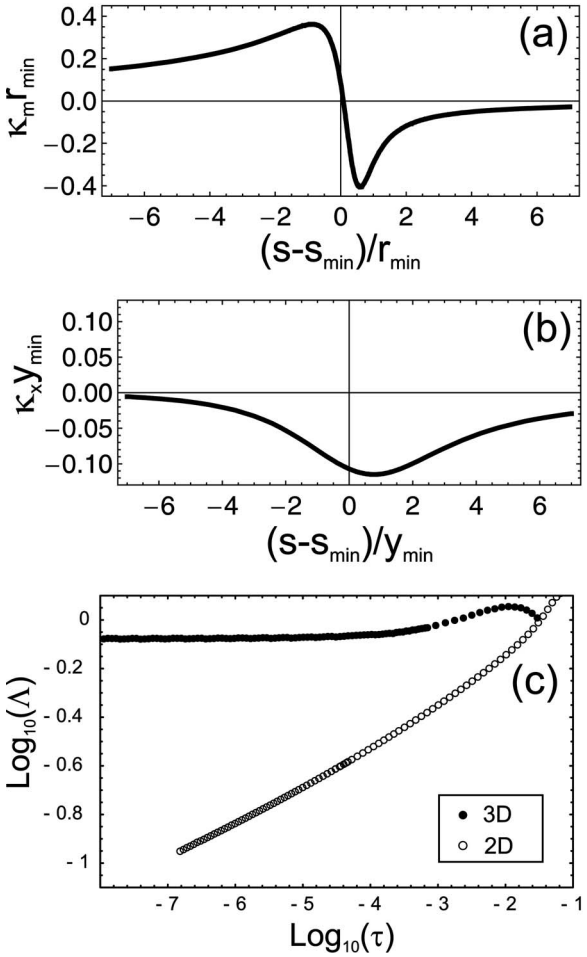

FIG. 3. (a) 3D mean curvature (κ_m) as a function of arc-length s near the pinching region at a time near the singularity. The variables are made dimensionless by r_{min}. The curvature at the minimum is positive, and the curvature (which determines the sign of the Laplace pressure) changes sign near the minimum. (b) 2D curvature (κ_x) as a function of arc-length near the pinching region at a time near the singularity. The variables are made dimensionless by y_{min}. The curvature is always negative near y_{min}, meaning the curvature always tends to increase the neck diameter. (c) Data plotted of the vertical to horizontal length scale ($\Lambda = \kappa_x y|_{y=y_{min}}$ in 2D, $\Lambda = \kappa_z r|_{r=r_{min}}$ in 3D) of the pinch region for both 3D axisymmetric pinch-off (full circles) and 2D fluid sheet pinch-off (open circles). In 3D, this aspect ratio approaches an asymptotic constant value, indicating that the pinch profile maintains a universal shape. In 2D, the neck thickness shrinks faster than the curvature, so that the neck becomes "slender" as $\tau=0$ is approached.

where $h(x,t)$ is the boundary profile of the drop. A mathematical description of this simplification can be found in Refs. 17 and 18, and the resulting equations in the inviscid limit for the boundary profile $h(x,t)$ and the velocity $v(x,t)$ are

$$\frac{\partial h}{\partial t} + \frac{\partial}{\partial x}(hv) = 0, \tag{9}$$

$$\frac{\partial v}{\partial t} + v\frac{\partial v}{\partial x} - \frac{\lambda}{\xi}\frac{\partial^3 h}{\partial x^3} = 0. \tag{10}$$

Such 1D "slender" approximations have been used many times in the past to calculate self-similar solutions of pinching singularities.[2,4,17,19,20] Starting from different initial conditions, we have found solutions to Eqs. (9) and (10) that contain a finite time singularity where $h(x,t)\to 0$ and $v(x,t)\to\infty$. To solve these equations, we used the "*N D Solve*" function in MATHEMATICA which is based on the method of lines. Since these partial differential equations are meant to describe 2D pinch-off near the singularity, the appropriate boundary conditions should contain a nonzero initial velocity to account for the Bernoulli suction observed in the boundary-integral simulations. We propagated the solutions of Eqs. (9) and (10) using many different boundary conditions, and all sets that resulted in finite-time pinch-off were qualitatively the same and displayed the same scaling exponents. Subsequently, we choose to discuss one such case in the range $0<x<2$ with $\lambda=1$ and $\xi=1$ and the following set of boundary conditions:

$$\begin{aligned} &h(x,0) = 1 - 0.2\cos(\pi x/2), \\ &v(x,0) = \pi\sin(\pi x/2), \\ &\frac{\partial h(0,t)}{\partial x} = 0, \\ &\frac{\partial h(2,t)}{\partial x} = 0, \\ &v(0,t) = 0, \\ &v(2,t) = 0. \end{aligned} \tag{11}$$

The solution for $h(x,t)$ with these boundary conditions is shown for multiple times during the evolution in Fig. 4(a). Figure 4(b) shows $h(x,t)$ at time very near the singularity. The position of the minimum thickness (x_{min}, h_{min}) not only collapses towards $h_{min}=0$, but also moves towards a finite value of $x_{min}\sim 0.995$. In order to ensure adaptive time stepping and spatial mesh refinement as the singularity is approached, "*N D Solve*" was stopped at various time intervals near the singularity, and the spatial grid of x values were redistributed according to the same regridding technique used for the boundary integral simulations [Eq. (8)], at which point the routine was restarted. The time intervals between regridding became smaller as the singularity was approached. 500 points were used during most time intervals, although points were added for times $\tau<10^{-7}$, ending in approximately 700 points on the spatial grid when the routine was halted at $\tau=10^{-10}$. The time step was maintained at a fraction 10^{-4} of each time interval between each spatial regridding. The solutions were followed until $\tau\sim 10^{-10}$, where the minimum neck height $h_{min}\sim 10^{-7}$. Figure 5 shows a Log_{10}-Log_{10} plot of h_{min} versus τ and $x_{min}-x_o$ versus τ, indicating a best fit power law exponent of 0.7476 ± 0.005 and 0.6869 ± 0.005, respectively. To illustrate the self-similar nature of the singularity, we rescale the profile at different times very near pinch-off using the fitted power law exponents for the horizontal and vertical direction (Fig. 6). The scaled data for the profiles then collapse onto a single curve over several orders of magnitude change in τ.

Although these partial differential equations are nonlinear, solutions are much more easily calculated than the full

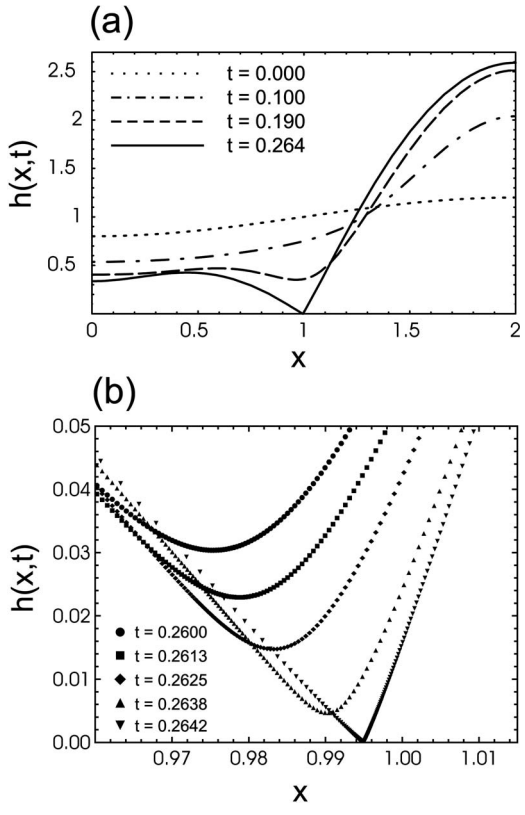

FIG. 4. (a) Plot of the profile of a 2D drop $h(x,t)$ as a function of x showing the evolution of $h(x,t)$ for several values of t up to the singular point $t \sim 0.264$ starting from the initial conditions given in Eq. (11) at $t=0$. (b) High magnification view of the behavior of $h(x,t)$ as a function of x for five different times very close to the moment of pinch-off. Note that the minimum thickness ($h_{\min}$) approaches the singularity in both the vertical and horizontal directions. The variation of each of these quantities is characterized by a different exponent, as shown in Figs. 5 and 6.

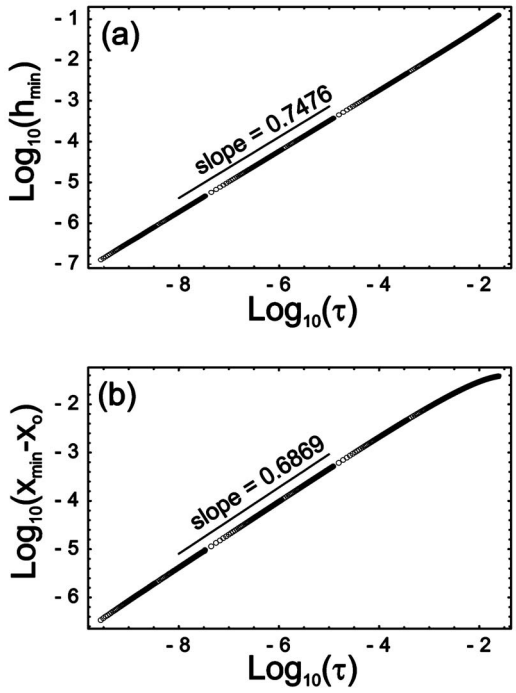

FIG. 5. Log_{10}-Log_{10} plots of (a) $h_{\min}(\tau)$ and (b) $x_{\min}(\tau)-x_o$ obtained by solving the set of partial differential equations (9) and (10) with the boundary conditions in Eq. (11). The value of τ was chosen by a best power law fit to the data. The open circles denote data and the solid line denotes the slope.

boundary integral solutions. For example, following the solutions of Eqs. (9) and (10) over 8 orders of magnitude in time took only 5–10 min, as opposed to 5 days required to solve Eqs. (1) and (2). Although the exponent for the minimum neck thickness was slightly different than the one obtained from the solutions of the PDEs (0.7516 as opposed to 0.7476), this difference is most likely explained by the fact that the pinch shape has not yet reached the slender limit in Fig. 2, with an aspect ratio of 1:10 in the horizontal and vertical length scales (Fig. 3).

Equations (9) and (10) have been examined by previous authors,[18,21] with the assumption that the similarity exponent for pinching solutions should be 2/3. Numerical results in Ref. 21 reports a power law exponent for $h_{\min}$ versus τ of $\alpha=0.74$. However, the deviations from 2/3 are attributed to the finite range of the simulation in τ or neglecting higher-order terms in the equations. In another case, similar deviations from the expected value 2/3 were obtained from numerical solutions of nearly identical equations[17] for studies of finite-time singularities in Hele-Shaw systems with zero fluid density and a finite fluid density. They found that with a finite fluid density, the viscous terms become negligible near pinch-off and power law exponents for various quantities are nearly identical to ones that we have found. For example, Dupont *et al.*[17] reported on an exponent of 0.766 ± 0.05 for the minimum neck radius. Although their numerical values for the exponents are similar to ours, they attribute the deviation from the dimensional analysis result $\alpha=2/3$ to logarithmic corrections. Our results from the boundary-integral simulations show that there is true power law behavior, but with an irrational exponent.

IV. CALCULATION OF THE SELF-SIMILAR EXPONENT

Equations involving self-similar solutions of the second kind have been used to describe a variety of phenomena including nonlinear diffusion and heat conduction, filtration-absorption and flow through porous media,[22] and viscous

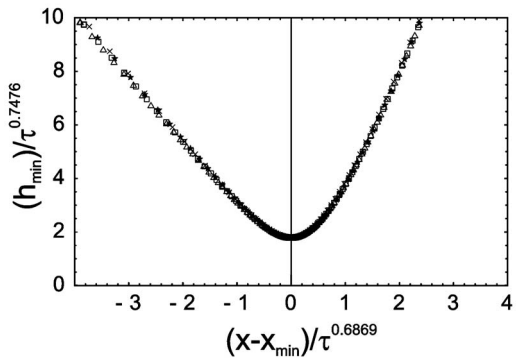

FIG. 6. Scaled plots of the pinch-off region at different values of τ. The data come from the solutions of the partial differential equations (9) and (10) with the boundary conditions in Eq. (11). The symbols denote the following values of τ: $\Delta=1.21\times10^{-5}$, $\square=1.13\times10^{-6}$, $\star=3.38\times10^{-8}$, and $\times=3.76\times10^{-9}$. In order for the profiles to collapse onto a single curve, the horizontal and vertical axes must be scaled by different exponents, obtained from Fig. 5.

gravity currents.[23] Finding the numerical value of the self-similarity exponent typically involves solving a nonlinear eigenvalue problem, where the boundary conditions are given at different points and a "shooting" method is required to find the solution between them. For 2D inviscid pinch-off, we begin with Eqs. (9) and (10) and define a new function $g(x,t)=(\lambda/\xi)h(x,t)$ in order to remove the fluid parameters from the problem. Equations (9) and (10) then become

$$\frac{\partial g}{\partial t}+\frac{\partial}{\partial x}(gv)=0, \tag{12}$$

$$\frac{\partial v}{\partial t}+v\frac{\partial v}{\partial x}-\frac{\partial^3 g}{\partial x^3}=0. \tag{13}$$

Next, we assume a self-similar form for both $g(x,t)$ and $v(x,t)$,

$$g(x,t)=\frac{(x_o-x)^4}{(t_o-t)^2}G(\eta),$$
$$v(x,t)=\frac{(x_o-x)}{(t_o-t)}V(\eta), \tag{14}$$

where η is the similarity variable

$$\eta=\frac{(x_o-x)}{\gamma(t_o-t)^\alpha} \tag{15}$$

and (x_o,t_o) is the spatial/temporal position where the singularity occurs. This self-similar form illustrates the relation between the similarity exponent α, and the various exponents of singular quantities, such as $g_{\min}$ and $v_{\min}$. For example, if we follow the minimum neck height in time, this occurs at $x=x_{\min}(t)=A(t_o-t)^\alpha+x_o$, where A is a constant determined by the initial conditions leading up to pinch-off. Plugging this into Eq. (14), we find that $h_{\min}(t)=A^4(t_o-t)^{4\alpha-2}G(A/\gamma)$. So this implies that $h_{\min}$ follows a power law in time with an exponent of $4\alpha-2$. We should note that if the similarity exponent was in fact 2/3 as predicted by dimensional analysis, then $4(2/3)-2=2/3$, and $h_{\min}$ would also follow a 2/3 power law.

In the following discussion, we will limit ourselves to solutions where $t<t_o$ (before pinch-off), so that positive and negative values of η refer to solutions where $x<x_o$ and $x>x_o$, respectively. Although the similarity exponent α has a universal value for self-similar solutions of 2D inviscid pinch-off, the value of γ cannot be obtained *a priori* and will depend on the initial conditions leading up to pinch-off. To calculate the value of α, we plug similarity solutions (14) into Eqs. (12) and (13) and obtain the following coupled set of ordinary differential equations:

$$\frac{G'}{G}=\frac{5V+\eta V'-2}{\eta(\alpha-V)}, \tag{16}$$

$$V(V-1)+\eta V'(V-\alpha)=24G+\eta 36G'+12\eta^2G''+\eta^3G''', \tag{17}$$

where the prime (e.g., G') notation denotes differentiation with respect to η. The functions $G(\eta)$ and $V(\eta)$ cannot be determined without first specifying the value of γ, which is included in the definition of η. For this reason, it is convenient to eliminate the explicit dependence on η and reduce the equations to an autonomous form, similar to the method used in Ref. 23. To do this, we make the substitution of the dependent variable $\nu=\ln(|\eta|)$ and write the equations in terms of $G(\nu)$ and $V(\nu)$,

$$\frac{G'}{G}=\frac{5V+V'-2}{(\alpha-V)}, \tag{18}$$

$$V(V-1)+V'(V-\alpha)=24G+26G'+9G''+G''', \tag{19}$$

where the prime now denotes differentiation with respect to ν. The phase space representation is constructed using G as the independent variable, and defining the derivatives of G as new functions $P(\nu)=G'(\nu)$, and $Q(\nu)=G''(\nu)$. After a little algebra, we obtain three first-order ODEs for the functions V, P, and Q, as a function of G,

$$\frac{dV}{dG}=\frac{\alpha-V}{G}+\frac{2-5V}{P}, \tag{20}$$

$$\frac{dP}{dG}=\frac{Q}{P}, \tag{21}$$

$$\frac{dQ}{dG}=-26-\frac{(\alpha-V)^2}{G}+\frac{-2(12G+\alpha)+V(1+5\alpha-4V)-9Q}{P}. \tag{22}$$

The appropriate boundary conditions for V, P, and Q can be determined by considering the limits of $\eta\to 0$ and $\eta\to\pm\infty$ of the self-similar forms in Eq. (14). The limit $\eta\to 0$ refers to $x\to x_o$ with a finite t. When $x\to x_o$, $g(x,t)$ must also be a finite number if the profile of the pinch is to remain smooth. The only way this can happen is to require $G\sim\eta^{-4}\sim e^{-4\nu}$ as $\eta\to 0$. The same holds true for the velocity V so that $V\sim\eta^{-1}\sim e^{-\nu}$ as $\eta\to 0$. This means that both G and V diverge to infinity as $\eta\to 0$ ($\nu\to-\infty$). The limit that $\eta\to\pm\infty$ refers to $t\to t_o$ while x is held fixed. Then $g(x,t)$ and $v(x,t)$ must also be finite in this limit so that $G\sim\eta^{-2/\alpha}\sim e^{-2\nu/\alpha}$ and $V\sim\eta^{-1/\alpha}\sim e^{-\nu/\alpha}$ as $\eta\to\pm\infty$ ($\nu\to\infty$). These asymptotic forms imply the following behavior for the phase-space equations in the vicinity of the singular points at $G=0$ and $G=\infty$,

$$V\sim G^{1/4};\quad P\sim G;\quad Q\sim G\quad G\to\infty,$$
$$V\sim G^{1/2};\quad P\sim G;\quad Q\sim G\quad G\to 0. \tag{23}$$

Prior to pinch-off, the profile $g(x,t)$ must be continuous and positive, so we require $0<G<\infty$. The asymptotic expansions around the singular points $G=0$ and $G=\infty$ can be obtained using the lowest power in G from 23. Near $G=0$ we have

$$V\sim a_0G^{1/2}+\sum_{j=1}^{\infty}a_jG^{1/2+j/2}, \tag{24}$$

$$P \sim \frac{-2}{\alpha} G + \sum_{j=1}^{\infty} b_j G^{1+j/2}, \tag{25}$$

$$Q \sim \frac{4}{\alpha^2} G + \sum_{j=1}^{\infty} c_j G^{1+j/2}. \tag{26}$$

By inserting this expansion into Eqs. (20)–(22), and equating terms of equal powers in G, we find that all of the coefficients (a_j, b_j, c_j) can be determined by choosing α and one leading order term (e.g., a_0), so that the problem is reduced to a two parameter family of solutions. Near $G=\infty$, the expansion is

$$V \sim k_0 G^{1/4} + \sum_{j=1}^{\infty} k_j G^{1/4-j/4}, \tag{27}$$

$$P \sim -4G + m_1 G^{3/4} + m_2 G^{1/2} + \sum_{j=3}^{\infty} m_j G^{1-j/4}, \tag{28}$$

$$Q \sim 16G + \sum_{j=1}^{\infty} n_j G^{1-j/4}. \tag{29}$$

Inserting this expression into the ODEs for V, P, and Q leads to a four parameter family of solutions (e.g., α, k_0, m_1, m_2) where specifying three of the coefficients and α will determine all remaining coefficients (k_j, m_j, n_j). There are two solutions for each function V, P, and Q in the phase space, one corresponding to positive values of η and one to negative values of η. To generate a curve in the phase space corresponding to positive η solutions we need to specify four coefficients and α $(a_0^+, k_0^+, m_1^+, m_2^+, \alpha)$ for a total of five parameters. Then to generate the phase space curve corresponding to negative η solutions, we need only four more parameters since α has already been specified $(a_0^-, k_0^-, m_1^-, m_2^-, \alpha)$. This is a grand total of 9 parameters. Three boundary conditions come from the fact that $\partial g(x,t)/\partial x$, $\partial^2 g(x,t)/\partial x^2$, and $v(x,t)$ must be continuous at $x=0$ $(G=\infty)$, which implies the following relations between the leading terms in the asymptotic expansions:

$$k_0^- = -k_0^+,$$

$$m_1^- = -m_1^+, \tag{30}$$

$$m_2^- = m_2^+.$$

The nonlinear eigenvalue problem which determines α consists of finding the unique integral curve which connects the singular point at $G=0$, $\eta=+\infty$ and the singular point corresponding to $G=0$, $\eta=-\infty$ which satisfies the conditions of Eq. (30) near $G=\infty$. The eigensolution was found by numerically minimizing an objective function of the six parameters which define an integral curve which was constructed to have a minimum for the desired solution. In particular, values were chosen for α, the two parameters which determine the asymptotic solutions near $G=0$, $\eta=\pm\infty$, and the 3 parameters which define the series solution near $G=\infty$. The asymptotic series solutions were used to compute values of V, P, and Q for $0<G<10^{-3}$ for both the positive and negative η. These solutions were numerically integrated up to $G=10^3$ using the "*N D Solve*" function in MATHEMATICA. The difference between the values at $G=10^3$ obtained in this way and those obtained from the series solution valid near $G=\infty$ were minimized in the least squares sense using a global minimization technique (the MATHEMATICA function "*N Minimize*"). The minimization was started from multiple points in the 6 parameter space in order to prevent accidental trapping in a local minimum. The value of the self-similar exponent at the global minimum was found to be $\alpha = 0.6869 \pm 0.0003$, where the error represents the standard deviation of the values obtained from various initial sets of parameters. Thus the value of the power law exponent associated with $h_{\min}$ versus τ is $4\alpha - 2 = 0.7476 \pm 0.0012$. The numerical solution of the governing partial differential equations (Fig. 5) is in excellent agreement with our calculated value of α. We have composed a table (Table I) of power law exponents associated with various quantities such as curvature, velocity, etc. in order to compare to the exponents reported in Ref. 19 that were calculated from fits to their data. The functions $G(\eta)$ and $V(\eta)$ cannot be computed without first choosing the constant γ, but we can calculate V as a function of G from the solutions to Eqs. (20)–(22). By dividing $g(x,t)$ and $v(x,t)$ by appropriate powers of $(x_o - x)$ and $(t_o - t)$, we obtain values of G and V along the boundary. These data are plotted in Fig. 7 at a time $\tau = 3.76 \times 10^{-9}$, along with the function $V(G)$ found from the global minimization technique. It should be noted that the point $(x_{\min} - x_o, g_{\min})$ always occurs at $G \sim 0.63$.

TABLE I. Power law exponents (τ^β) associated with various quantities near pinch-off. The subscript "min" denotes the value of the quantity at the position of the minimum neck thickness. The relationship to the similarity exponent α is shown in the last column.

Quantity	β	Relation to α
$h_{\min}$	0.7477 ± 0.0012	$4\alpha - 2$
$x_{\min} - x_o$	0.6869 ± 0.0003	α
$v_{\min}$	-0.3131 ± 0.0003	$\alpha - 1$
$\kappa_{\min}$	-0.6261 ± 0.0006	$2\alpha - 2$

V. CONCLUSIONS

We have investigated the pinch-off of a 2D droplet of inviscid fluid using several numerical techniques and compared the results to the well-known solutions in 3D. Although line tension always tends to stabilize a 2D region and drive it toward a circular shape, a sufficiently distorted region will nevertheless undergo pinch-off due to nonlinear Bernoulli effects. In contrast to 3D, the 2D pinch-off process is described by a self-similar solution of the second kind, which is characterized by a memory of the initial conditions on the solution and an anomalous scaling exponent. This self-similar solution is seen in boundary-integral simulations of 2D potential flow. As the neck region shrinks, the horizontal and vertical lengths scale with different exponents so that the pinch region eventually becomes slender, allowing a sim-

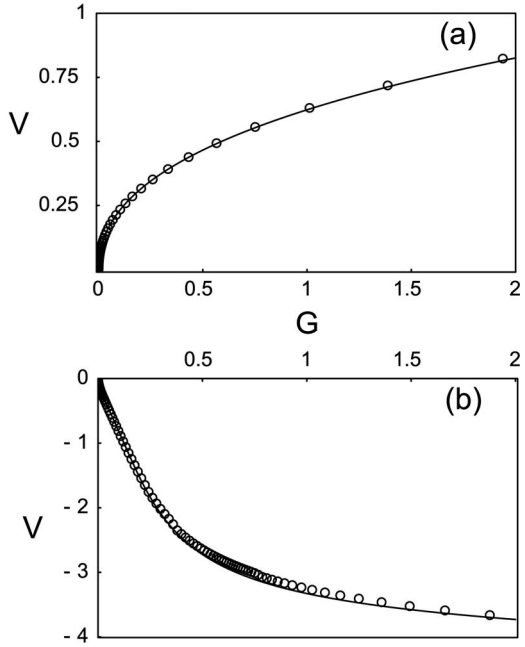

FIG. 7. Phase-space plots of the similarity function V as a function of G. The data points are calculated from the solutions of the partial differential equations (9) and (10) with the boundary conditions in Eq. (11). Starting from Eq. (14), we first calculate G and V by dividing the PDE solutions by appropriate powers of $(x-x_o)$ and $(t-t_o)$. The positive V curve (a) corresponds to $x<0$, and the negative V curve (b) corresponds to $x>0$. The solid line is the calculated phase-space curves $V(G)$ from Eqs. (20)–(22).

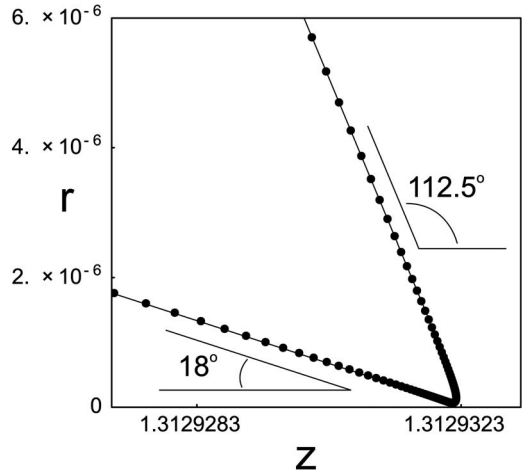

FIG. 8. Close-up of the singular region from 3D axisymmetric droplet simulation depicted in Fig. 2(b). The universal shallow and steep cone angles of 18° and 112.5° are shown on each side of the singularity. Reproduction of these cone angles is a check on our numerical routine since they have been realized by previous authors.

plification of the governing equations in the form of a 1D coupled set of partial differential equations for the neck profile $h(x,t)$ and the velocity $v(x,t)$. We have solved these PDEs and observed the self-similar solution starting from many different initial conditions. Furthermore, using a phase space formalism similar to that in Ref. 23 we have constructed a nonlinear eigenvalue problem which yields the anomalous similarity exponent $\alpha=0.6869\pm0.0003$. Other exponents of physical interest are all related to α; for example the exponent which governs the time dependence of the minimum neck diameter is $4\alpha-2=0.7477$. Because of the widespread applicability of the slender approximation, the asymptotic solutions we have identified may be useful in other investigations.

One of the primary motivations for this work was to understand the results of recent experiments in our lab on pinch-off and coalescence of quasi-2D liquid lenses.[13] Although liquid lens systems are considerably more complicated than both the 2D and 3D inviscid pinch-off cases discussed in this paper, we have found some flow regimes which generate pinch-off profiles that bear a striking resemblance to our 2D calculations; results of this work will be published elsewhere.

APPENDIX: VERIFICATION OF BOUNDARY INTEGRAL CODE

Small oscillations of droplets in 3D and 2D provide a useful check of the numerical scheme used in the solution of the boundary integral equations of potential flow because exact solutions are known. Simulations were started from rest $(\vec{\mathbf{v}}=0)$ with the following small distortions on a sphere or circle of radius R_o with the perturbation in the first quadrant given by:

3D drops,

$$Z(j)=\{1+\epsilon P_m[\cos(j)]\}\sin(j),$$
$$R(j)=\{1+\epsilon P_m[\cos(j)]\}\cos(j), \tag{A1}$$

2D sheets,

$$X(j)=[1+\epsilon\cos(mj)]\sin(j),$$
$$Y(j)=[1+\epsilon\cos(mj)]\cos(j), \tag{A2}$$

where $0\leqslant j\leqslant\pi/2$ is the parametric surface coordinate and P_m is the Legendre polynomial of order $m\geqslant 2$. Simulations were performed for $m=2,4,6$ with $\epsilon=0.02$ and $N=40$ marker points along the boundary. The observed frequencies were always within 0.1% of the values obtained by linear theory,[24]

$$\omega_{3D}^2=m(m-1)(m+2)\frac{\sigma}{\rho R_o^3},$$
$$\omega_{2D}^2=m(m^2-1)\frac{\lambda}{\xi R_o^3}. \tag{A3}$$

Another useful check of the numerical routine is provided by comparison of our results for pinch-off in 3D axisymmetric drops to previously published results.[7–9] Near pinch-off for inviscid 3D axisymmetric drops, the singular region approaches a double-cone profile with cone angles that are universal. The cone half-angles are approximately 18° for the shallow cone and 112.5° for the overturned, steep cone. Figure 8 shows the results from one of our 3D simulations near pinch-off. The cone angles that we measure are in excellent agreement with the previous predictions.

[1]J. Eggers, "Drop formation: An overview," Z. Angew. Math. Mech. **85**, 400 (1997).
[2]J. Eggers, "Universal pinching of 3D axisymmetrical free-surface flow," Phys. Rev. Lett. **71**, 3458 (1993).
[3]G. I. Barenblatt, *Scaling, Self-Similarity, and Intermediate Asymptotics* (Cambridge University Press, Cambridge, 1996).
[4]D. T. Papageorgiou, "On the breakup of viscous-liquid threads," Phys. Fluids **7**, 1529 (1995).
[5]J. Eggers, "Nonlinear dynamics and breakup of free-surface flows," Rev. Mod. Phys. **69**, 865 (1997).
[6]Y.-J. Chen and P. Steen, "Dynamics of inviscid capillary breakup: Collapse and pinchoff of a film bridge," J. Fluid Mech. **341**, 245 (1997).
[7]R. F. Day, E. J. Hinch, and J. R. Lister, "Self-similar capillary pinchoff of an inviscid fluid," Phys. Rev. Lett. **80**, 704 (1998).
[8]D. Leppinen and J. R. Lister, "Capillary pinch-off in inviscid fluids," Phys. Fluids **15**, 568 (2003).
[9]N. Monika and P. H. Steen, "Numerical simulations of inviscid capillary pinchoff," J. Comput. Phys. **200**, 299 (2004).
[10]J. C. Burton, J. E. Rutledge, and P. Taborek, "Fluid pinch-off dynamics at nanometer length scales," Phys. Rev. Lett. **92**, 244505 (2004).
[11]J. C. Burton, J. E. Rutledge, and P. Taborek, "Fluid pinch-off in superfluid and normal ^{4}He," Phys. Rev. E **75**, 036311 (2007).
[12]A. U. Chen, P. K. Notz, and O. A. Basaran, "Computational and experimental analysis of pinch-off and scaling," Phys. Rev. Lett. **88**, 174501 (2002).
[13]J. C. Burton and P. Taborek, "Role of dimensionality and axisymmetry in fluid pinch-off and coalescence," Phys. Rev. Lett. **98**, 224502 (2007).
[14]C. Pozrikidis, *Introduction to Theoretical and Computational Fluid Dynamics* (Oxford University Press, New York, 1997).
[15]Q. Nie and G. Baker, "Application of adaptive quadrature to axisymmetric vortex sheet motion," J. Comput. Phys. **143**, 49 (1998).
[16]P. K. Notz, A. U. Chen, and O. A. Basaran, "Satellite drops: Unexpected dynamics and change of scaling during pinch-off," Phys. Fluids **13**, 549 (2001).
[17]T. F. Dupont, R. E. Goldstein, L. P. Kadanoff, and S. Zhou, "Finite-time singularity formation in Hele-Shaw systems," Phys. Rev. E **47**, 4182 (1993).
[18]L. Ting and J. B. Keller, "Slender jets and thin sheets with surface-tension," SIAM J. Appl. Math. **50**, 1533 (1990).
[19]P. Constantin, T. F. Dupont, R. E. Goldstein, L. P. Kadanoff, M. J. Shelley, and S. M. Zhou, "Droplet breakup in a model of the Hele-Shaw cell," Phys. Rev. E **47**, 4169 (1993).
[20]A. L. Bertozzi, M. P. Brenner, T. F. Dupont, and L. P. Kadanoff, "Singularities and similarities in interface flows," in *Trends and Perspectives in Applied Mathematics*, Applied Mathematical Sciences, Vol. 100, edited by L. Sirovich (Springer-Verlag, Berlin, 1994), p. 155.
[21]M. C. Pugh and M. J. Shelley, "Singularity formation in thin jets with surface tension," Commun. Pure Appl. Math. **51**, 733 (1998).
[22]G. I. Barenblatt, M. Bertsch, A. E. Chertock, and V. M. Prostokishin, "Self-similar intermediate asymptotics for a degenerate parabolic filtration-absorption equation," Proc. Natl. Acad. Sci. U.S.A. **97**, 9844 (2000).
[23]J. Gratton and F. Minotti, "Self-similar viscous gravity currents—Phase-plane formalism," J. Fluid Mech. **210**, 155 (1990).
[24]H. Lamb, *Hydrodynamics* (Cambridge University Press, Cambridge, 1932).